


# Polarization-independent high- $Q$ monolayer Ge-assisted near-perfect absorber through quasibound states in the continuum

Kedi Wu<sup>①,\*†</sup>, Haosen Zhang<sup>①,\*</sup>, and Guo Ping Wang<sup>①,‡</sup>

State Key Laboratory of Radio Frequency Heterogeneous Integration, College of Electronics and Information Engineering, Shenzhen University, Shenzhen 518060, China

 (Received 26 April 2023; revised 26 June 2023; accepted 28 July 2023; published 8 August 2023)

Narrow-band metasurface perfect absorbers with a high-quality ( $Q$ ) factor play a vital role in governing the performance of optoelectronic devices. However, it is quite challenging to realize polarization-independent high- $Q$  perfect absorption at a near-infrared wavelength by only a single-layered structure without using the back reflectors. Here, we theoretically propose a monolayer high- $Q$  near-perfect metasurface absorber with unit cells comprised of four germanium (Ge) split rings. Based on quasibound states in the continuum, the Mie modes with low radiative decay rates are induced by the orientation of each split ring to match the low nonradiative decay rates and achieve high- $Q$  absorption performance. The high reflection background mode excited by four split rings can transform the symmetrically coupled Mie modes into asymmetrically coupled ones and decrease the radiative decay rate of transmission, enabling the monolayer structure to break through the absorption limit of 50% to near 100%. We have theoretically demonstrated that the maximum absorption of the presented structure is as high as 93% at 1530 nm of the  $Q$  factor up to 470. The structure is polarization independent due to its  $C_4$  symmetry. Our proposed monolayer all-dielectric metasurface without any back reflectors achieves near-perfect absorption at a very narrow bandwidth. This work may provide a paradigm for designing polarization-independent high- $Q$  monolayer perfect absorbers, which is potentially applicable in ultrafast optoelectronic devices and integrated photon systems.

DOI: [10.1103/PhysRevB.108.085412](https://doi.org/10.1103/PhysRevB.108.085412)

## I. INTRODUCTION

Metasurface perfect absorbers (MPAs), which are employed to efficiently absorb light waves in a specific spectral range, have drawn a great deal of attention due to their promising potential in photovoltaic devices and optoelectronic systems [1–3]. According to the absorption spectral bandwidth, MPAs can be classified as narrow-band and broadband absorbers [3,4]. Narrow-band MPAs with a high- $Q$  factor play essential roles in sensing [3] and light emission fields [5]. With the help of plasmon resonances, plasmonic MPAs could be impedance matched to the surrounding environment to achieve high- $Q$  near-perfect absorption [3,6,7]. However, metallic units of the plasmonic MPAs generate considerable heat instead of photocarriers due to a significant portion of absorption taking place in metallic units and the large intrinsic loss of metals in the visible and near-infrared wavelength ranges [8]. This drawback might degrade the absorption performance of the developed optoelectronic devices. The all-dielectric MPAs with low intrinsic loss have been proposed as alternatives to plasmonic ones [8–10]. Multiordered Mie resonance modes are supported by the all-dielectric MPAs for enhancing absorption [4,10]. The absorption could be realized when the radiative decay rate of Mie resonances and the nonradiative decay rate of dielectrics are matched,

which is referred to as a critical coupling condition [11]. The absorption bandwidth is determined by the sum of radiative and nonradiative decay rates. However, these designs need to increase the nonradiative decay rate to match the significant radiative decay rate of Mie resonances, which enhances the absorption but simultaneously decreases the  $Q$  factor [8,10]. The  $Q$  factors of these absorbers are as low as 10. Therefore, the critical point to achieving high- $Q$  absorption in all-dielectric absorbers is to reduce both radiative and nonradiative decay rates [11].

Recently, the bound states in the continuum (BICs) have attracted significant attention in the all-dielectric metasurfaces as they open more degrees of freedom to tune the radiative decay rate to achieve high- $Q$  absorption [12–15]. Ideal BICs, which cannot be directly excited, are completely confined states without any radiation characterized by an infinite  $Q$  factor and vanishing linewidth [16,17]. By tailoring the in-plane symmetry within each unit cell of the all-dielectric metasurfaces, ideal BICs can be transformed into  $Q$ BICs, which can radiate to the external continuum [17]. As well, for a monolayer structure with mirror symmetry, the high- $Q$  Mie resonances with low radiative decay rates could be excited by breaking structural symmetries such as translating and/or orientating the nanoparticles of the unit cell to achieve high- $Q$  absorption [13–16]. However, the maximum absorption  $A_{\max}$  is only 50% at the critical coupling point in this kind of structure due to the excitation of only one resonance mode. To break through the absorption limit of 50% in monolayer structures, a way to excite two high- $Q$  Mie modes with degenerate frequency but opposite symmetry has been proposed [11,18].

\*These authors contributed equally to this work.

†kdwu@szu.edu.cn

‡Corresponding author: gpwang@szu.edu.cn

By introducing a superstrate with a refractive index close to the substrate at a monolayer structure and adjusting the period, the magnetic dipole (MD) and electric dipole (ED)  $QBIC$  resonances, which meet critical coupling at respective resonant wavelengths, could be spectrally overlapped to overcome the absorption limit of 50% [18]. However, the absorption performance of these absorbers is highly sensitive to the geometric parameters of the structures. The high- $Q$  ED and MD modes may be excited at different wavelengths due to slight fabrication errors, which may significantly reduce the absorption performance of the structures. Another issue is that the maximum absorption of these absorbers would be limited (about 80%). This limitation is because it is difficult to meet the critical coupling of both ED and MD modes at the same wavelength simultaneously. Adding a metallic mirror at the bottom of the monolayer structures can also break through the absorption limit of 50%. The metallic mirror turns the structures from two-port systems into one-port systems, hence the transmission being eliminated [19–21]. The low-index lossless dielectric spacer separates the resonators and metallic mirrors. The reflection of the front of the resonators can be canceled by the excited wave in the cavity formed by the resonators, spacer, and metallic mirror [20]. In this way, the metallic layer absorbs a portion of light waves and introduces non-negligible heat, which may degrade their absorption performance at high pumping intensity. As alternatives to metallic mirrors, dielectric mirrors with low thermal conductivity and ohmic loss could be added at the bottom of the monolayer structures and can also achieve high- $Q$  near-perfect absorption [15]. However, the absorbers mentioned above need at least two layers for high- $Q$  perfect absorption due to they need a back reflector to suppress the transmission. Moreover, based on  $QBIC$ , high- $Q$  absorption performance is achieved by introducing a perturbation in the structural symmetry of the absorbers. Nevertheless, they are sensitive to the polarization of incident light, so their practical applicability may be limited [20,22]. Thus, there is still a challenge for the development of monolayer MPAs (MMPAs) that can achieve polarization-independent high- $Q$  near-perfect absorption without the back reflectors.

In this work, we propose a polarization-independent high- $Q$  near-perfect absorber based on an all-dielectric monolayer metasurface with unit cells comprised of four Ge split rings. Based on  $QBIC$ , the Mie modes with low radiative decay rates are induced by the orientation of each split ring to match the low nonradiative decay rates and achieve high- $Q$  absorption at the critical coupling point. The four split rings with the same geometric parameters can excite a high reflection background mode over a broad spectral range near the resonance wavelength of the Mie modes. The high reflection background mode transforms the Mie modes into asymmetrically coupled Mie modes and decreases the radiative decay rate of the transmission, enabling the monolayer structure to break through the absorption limit of 50%. We have theoretically and numerically demonstrated the maximum absorption of the presented monolayer structure is as high as 93% at 1530 nm, and the value of the  $Q$  factor is as high as 470. The  $C_4$  symmetry of the structure enables polarization independence under normal incidence. Our proposed monolayer structure without any back reflectors could achieve near-perfect absorp-

tion at a very narrow bandwidth. This work might provide an alternative strategy for designing polarization-independent high- $Q$  monolayer perfect absorbers, which may have excellent potential in sensing [5], photoelectric detecting [23], optical filtering [24], and lasing [25].

## II. DESIGNS OF MMPA TO BREAK THE ABSORPTION LIMIT

We start from a lossy dielectric ( $n = n_1 + in_2$ ) resonator coupled to two ports with the temporal coupled-mode theory (TCMT) to explore the conditions of perfect absorption in monolayer structure [10,26]. In the case that only a single resonance is excited in the resonator, based on the TCMT, the total absorption  $A$  at the angular frequency  $\omega$  of a single incident wave can be expressed as [10]

$$A = \frac{4\gamma_1\gamma_n}{(\omega - \omega_0)^2 + (\gamma_1 + \gamma'_1 + \gamma_n)^2}, \quad (1)$$

where  $\omega_0$  is the resonant angular frequency,  $\gamma_1$  and  $\gamma'_1$  are radiative decay rates into two different ports at the resonance (corresponding to reflection and transmission), and  $\gamma_n$  is the nonradiative decay rate, respectively. The total radiative decay rate (denoted as  $\gamma_r = \gamma_1 + \gamma'_1$ ) describes the leakage at the interface between the dielectric resonator and free space. The nonradiative decay rate originates from the intrinsic dissipation of lossy dielectric. Both radiative and nonradiative decay rates can be obtained from the electromagnetic fields of the structures either numerically or experimentally. Here, we numerically calculated fields and further get transmission and absorption spectra using the finite-difference time-domain (FDTD) method [27,28]. The total  $Q$  factor (denoted as  $Q$ ) of the lossy structure can be extracted from the numerically calculated absorption spectra. Then the sum of the radiative and nonradiative decay rates ( $\gamma_r + \gamma_n$ ) can be calculated by  $\gamma_r + \gamma_n = \omega_0/2Q$ . It is worth noting that  $\gamma_r$  is independent of the loss of material. As a result,  $\gamma_r$  can be extracted from the transmission spectra of the lossless structure, meaning the imaginary part of the refractive index of dielectric is neglected ( $n_2 = 0$ ). According to Eq. (1), the maximum light absorption of a resonator supporting a mirror-symmetric resonance ( $\gamma_1 = \gamma'_1$ ) will reach only 50% under critical coupling condition  $\gamma_n = \gamma_r$  [shown in Fig. 1(b)]. To overcome the limit of 50%, simultaneously exciting two degenerate critically coupled resonances with opposite symmetry has been proposed [11,18]. High absorption could be achieved when MD and ED resonances with the same radiative and nonradiative decay rates overlap (known as the degenerate critical coupling condition). Adding a back reflector, such as a metallic or dielectric mirror separated by a lossless dielectric spacer at the bottom of the resonator array, can also break through the absorption limit of 50% [15,19–21]. The back reflectors turn the structure from a two-port system into a one-port system ( $\gamma'_1 = 0$ ), and the transmission could be eliminated [18–20]. The reflection of the front of resonators can be suppressed at the critical coupling point.

For the resonator supporting asymmetrically coupled resonance ( $\gamma_1 \neq \gamma'_1$ ), the perfect absorption could be achieved in a monolayer structure when  $\gamma'_1 \ll \gamma_1$  and  $\gamma_n \approx \gamma_1$  even for only a single resonance. The ratio between  $\gamma_1$  and  $\gamma'_1$  can be

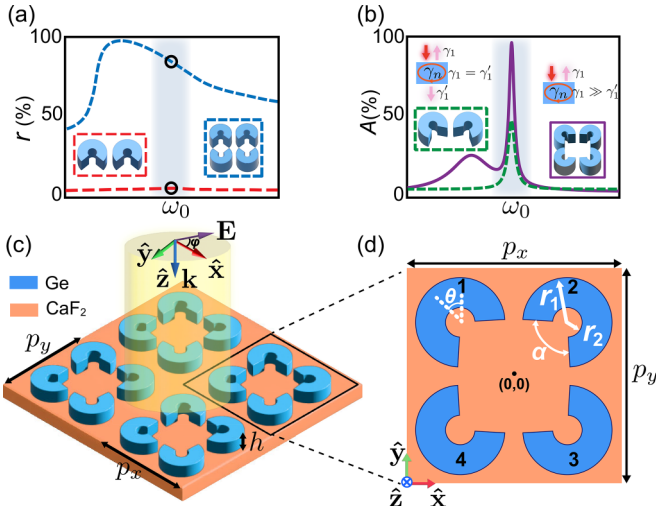


FIG. 1. (a), (b) Mechanism of the proposed high- $Q$  near-perfect absorption. The lossless structure ( $n_2 = 0$ ) composed of two and four split rings without a perturbation in the structural symmetry can provide a low and high reflection background over a broad spectral range, respectively. Based on  $QBIC$ , the monolayer lossy structure can excite the Mie modes with low radiative decay rates at  $\omega_0$  by the orientation of each split ring and achieve high- $Q$  absorption. For the structure composed of two split rings, the maximum absorption cannot break through the absorption limit of 50% due to no excitation of the high reflection background mode excited by the structure composed of four split rings transforms the symmetrically coupled Mie modes ( $\gamma_1 = \gamma'_1$ ) into asymmetrical ones ( $\gamma_1 \neq \gamma'_1$ ) and decreases  $\gamma'_1$ . This enables the monolayer structures to break the absorption limit of 50% at the critical coupling point. The gray shadows denote the bandwidths of the spectra. (c) Schematic of the monolayer Ge-assisted MPA. (d) Top view ( $\hat{x}$ - $\hat{y}$  plane) of the unit cell.

depicted by [10,26]

$$\frac{\gamma'_1}{\gamma_1} = 1 + 2\left(\frac{r}{t}\right)^2 + 2\left(\frac{r}{t^2}\right) \cos(\phi), \quad (2)$$

where real numbers  $r$  and  $t$  correspond to the amplitude of reflection and transmission coefficients of the background Fabry-Perot mode or low- $Q$  Mie mode, respectively. The relationship between  $r$  and  $t$  satisfies  $r^2 + t^2 = 1$  in the lossless structures ( $n_2 = 0$ ). The phase difference of the reflected electric field between background mode and resonance mode is defined as  $\phi = \phi_1 - 2\phi_2$ , where  $\phi_1$  and  $\phi_2$  are the phases of the complex reflection coefficients of background mode and resonance mode, respectively. In this work, all parameters in Eq. (2) are obtained in the lossless structures due to  $\gamma'_1$  and  $\gamma_1$  being independent of the loss of material. The parameters on the right-hand side of Eq. (2) can be calculated using the FDTD method. In Eq. (2), if  $r = 0$ , we can see that a symmetrically coupled resonator and the maximum absorption is 50%. It can be derived from Eq. (2) that the ratio between  $\gamma'_1$  and  $\gamma_1$  reaches a minimum while the  $\cos(\phi)$  approaches  $-1$  ( $\phi \approx 180^\circ$ ) to achieve perfect absorption. By substituting Eq. (2) into Eq. (1), the maximum absorption at resonance frequency can be obtained as  $A_{\max} = (1 + r)/2$ . Thus, a necessary condition for achieving perfect absorption is the high

reflection coefficient  $r$  of the background. The mechanism of near-perfect absorption achieved in monolayer structures is shown in Figs. 1(a) and 1(b). As shown in Fig. 1(a), the monolayer lossless structure composed of two split rings without a perturbation in the structural symmetry provides a low reflection background over a broad spectral range. By adding two split rings in a larger unit cell, the lossless monolayer structures composed of four split rings can support low- $Q$  Mie modes to provide a high reflection background. This high reflection background mode shows the same performance as the back reflectors in multilayer structures, rendering vastly different reflection and transmission. As shown in Fig. 1(b), based on  $QBIC$ , the Mie modes are excited at  $\omega_0$  for the lossy structures composed of two and four split rings by the orientation of each split ring. For the structure composed of two split rings, the maximum absorption cannot break through the absorption limit of 50% due to no excitation of the high reflection background mode near the absorption peak wavelength ( $r \approx 0$ ). The structure composed of four split rings supports high reflection coefficients  $r$  over a broad spectral range and transforms the symmetrically coupled Mie modes ( $\gamma_1 = \gamma'_1$ ) into asymmetrically coupled Mie modes  $\gamma_1 \neq \gamma'_1$ . This enables the monolayer structures to break the absorption limit of 50%. The absorption will be enhanced when the  $\cos(\phi)$  approaches  $-1$ , and perfect absorption can be achieved at the critical coupling point.

The total  $Q$  factor of the metasurface at resonance can be expressed as

$$Q = \left( \frac{1}{Q_r} + \frac{1}{Q_n} \right)^{-1}, \quad (3)$$

where  $Q_r = \omega_0/2\gamma_r$  and  $Q_n = \omega_0/2\gamma_n$  are the radiative and nonradiative  $Q$  factor, respectively. Thus, high- $Q$  performance requires simultaneous low nonradiative and radiative decay rates. Based on  $QBIC$ , an all-dielectric metasurface can achieve high- $Q$  absorption at resonant wavelength by tailoring the in-plane symmetry, as shown in Fig. 1(b). From the above discussion, we conclude that the high- $Q$  perfect absorption could be achieved in MMPAs if satisfying the three conditions: (1) the background mode has a high reflection coefficient  $r$  for high  $A_{\max}$ ; (2) the cosine of the phase difference of the reflected electric field between background mode and resonance mode approaches  $-1$ ; (3) the structure has small but nonzero nonradiative and radiative decay rates at the critical coupling point.

### III. PERFORMANCES OF THE MMPA

The details of our proposed MMPA are sketched in Figs. 1(c) and 1(d). Each unit cell consists of four Ge split rings with the same size but different orientations placed on the  $\text{CaF}_2$  ( $n_s = 1.426$ ) substrate with a thickness of  $1 \mu\text{m}$ . The period of this subwavelength structure is  $p_x = p_y = p = 1060 \text{ nm}$ . These four split rings are with outer radius  $r_1 = 213 \text{ nm}$ , inner radius  $r_2 = 66 \text{ nm}$ , height  $h = 239 \text{ nm}$ , and opening angle  $\alpha = 96^\circ$ , respectively. Figure 1(d) shows the top view of the unit cell on the plane. The four split rings are arranged at  $(-p/4, p/4)$ ,  $(p/4, p/4)$ ,  $(p/4, -p/4)$ , and  $(-p/4, -p/4)$ , respectively, being marked as SR1, SR2, SR3, and SR4, respectively. The unit cell shows mirror symmetry



in the  $\hat{x}$ – $\hat{y}$  plane. The orientation of each split ring is characterized by an orientation angle  $\theta$ , which is a critical parameter to switch the modes of metasurface between BICs and  $Q$ BICs. While  $\theta = 45^\circ$ , the  $C_4$  symmetry will be also introduced to the whole structure. Such a unit cell containing these four split rings can support the low- $Q$  Mie mode as a background mode, resulting in a high reflection coefficient over a broad spectral range [shown in Fig. 1(a)]. According to the grating law, this subwavelength structure has only the 0th-order reflection or transmission propagating modes, while the other higher diffraction orders are suppressed [29,30]. The complex refractive index of Ge ( $n_{\text{Ge}} = n_1 + in_2$ ) is obtained from the Palik data [31], showing that Ge is a high refractive index medium with a small but nonzero absorption at a near-infrared wavelength. The resonator with a high refractive index ( $n_1$ ) can support multiordered Mie resonances for enhancing absorption. A small but nonzero absorption coefficient ( $n_2$ ) plays a crucial role in generating high- $Q$  absorption with a low nonradiative decay rate. We use the FDTD method to get the results of the performance of the proposed MMPA and further explore the absorption mechanism. Plane waves are normally incident onto the monolayer structures. The polarization angle  $\varphi$  is defined as the angle between the electric field vector and  $\mathbf{k} \times \hat{y}$ , where  $\mathbf{k}$  is the wave vector of the incident light. We first simulate the case that the electric field of the incident light is along the  $\hat{x}$  direction [the  $\varphi = 0^\circ$  case illustrated in Fig. 1(c)]. The spectral range in the simulation ranges 1480–1580 nm. The periodic boundary conditions are applied to the  $\hat{x}$  and  $\hat{y}$  directions, and the perfectly matched layers are used as the absorption conditions in the  $\hat{z}$  direction.

The blue solid line of Fig. 2(a) shows the FDTD simulated absorption spectrum of this MMPA. The spectral absorption is defined as  $A = 1 - R - T$ , where  $R$  and  $T$  depict the reflection and transmission, respectively. We can see that the near-perfect absorption occurs at 1530 nm. The  $Q$  factor here is defined as  $f_0/\Delta f$ , where  $\Delta f$  is the full width at half maximum of the resonance. The result shows that the  $Q$  factor reaches a high value of 470. A weak low- $Q$  absorption peak at 1509 nm also contributes to a high reflection background over a broad spectral range, transforming the resonances at 1530 nm into asymmetrically coupled resonances, and decreasing  $\gamma'_1$  when the  $\cos(\phi)$  approaches  $-1$  [shown in Fig. 2(c)]. This low- $Q$  background mode shows the same performance as the back reflectors in multilayer structures, renders vastly different reflection and transmission, and enhances the absorption at the resonance wavelength of 1530 nm. The maximum absorption reaches 93%, indicating that this monolayer structure can break through the absorption limit of 50%. As depicted by the red dotted line in Fig. 2(a), the absorption spectrum of the structure consisting of SR1 and SR2 ( $p_y = 530$  nm) demonstrates that the maximum absorption ( $A_{\text{max}} = 40\%$ ) cannot break through the absorption limit of 50% due to no excitation of low- $Q$  but high reflection background mode near the absorption peak wavelength (corresponding to the case of symmetrically coupled resonances). Figure 2(b) displays the absorption spectra of the proposed structure by changing the polarization angle  $\varphi$  from  $0^\circ$  to  $90^\circ$ . We found that the optical response of MMPA remains unchanged while polarization is varying. The polarization-independent optical response comes from the  $C_4$  symmetry of the unit cells of MMPA. This feature

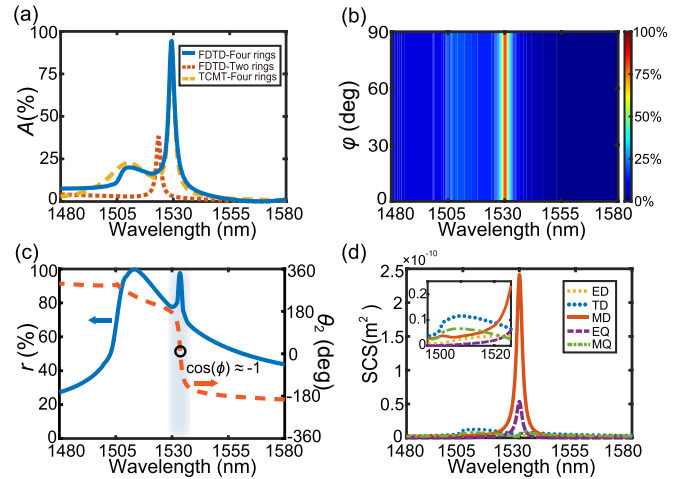


FIG. 2. (a) Simulated absorption spectra for the unit cell consisting of four (blue solid line) and two (red dotted line) split rings. The maximum absorption of MMPA is up to 93% at 1530 nm, and the  $Q$  factor is up to 470. The yellow dashed line denotes the absorption spectrum of the MMPA calculated using Eq. (1), derived based on TCMT. (b) Absorption spectra of the structure for varying polarization angle from  $0^\circ$  to  $90^\circ$ . This structure is polarization independent due to its  $C_4$  symmetry. (c) The amplitude (blue solid line) and phase (red dashed line) of reflection coefficient of the lossless structure. (d) Calculated SCSs of one unit cell in a metasurface. MD and EQ modes are simultaneously excited at 1530 nm, whereas the ED, TD, and MQ modes turn out to be weak. The inset shows the calculated SCSs at the wavelength range 1515–1555 nm. TD mode dominates at 1509 nm and provides a high reflection coefficient over a broad spectral range.

is particularly significant for designing optical devices and systems requiring stable functionality in different polarization states.

We use TCMT to provide an insightful analysis of the effect of high reflectance coefficient background mode on high- $Q$  near-perfect absorption in this monolayer structure. Figure 2(c) shows the amplitude (blue solid line) and phase (red dashed line) of the reflection coefficient of the lossless structure ( $n_2 = 0$ ). It can be seen that the lossless monolayer structure provides a high reflection coefficient and a low resonance phase  $\phi_2$  near the wavelength at 1534 nm, which can decrease  $\gamma'_1$  and enable the monolayer lossy structure to break through the absorption limit of 50%. The resonance wavelength of the lossless structure is slightly shifted from the lossy structure. The radiative and nonradiative decay rates are extracted from the numerically calculated transmission and absorption spectra of the structure. The total radiative decay rates ( $\gamma_1 + \gamma'_1$  in 1534 nm and  $\gamma_2 + \gamma'_2$  in 1509 nm) are extracted from the transmission spectrum of the lossless structure due to these parameters being independent of the loss of material. To get the radiative decay rates  $\gamma_1$  and  $\gamma'_1$ , the  $r$ ,  $t$ , and  $\phi_1$  have been obtained by fitting the real and imaginary parts of the reflection coefficient of the lossless structure. The value of  $\phi_2$  can be extracted from Fig. 2(c), which shows a low phase change in the reflected electric field at the resonance of 1534 nm. The ratio between  $\gamma_1$  and  $\gamma'_1$  can be calculated by Eq. (2). We then introduce material loss and obtain the

sum of the radiative and nonradiative decay rates ( $\gamma_{r1} + \gamma_{n1}$  and  $\gamma_{r2} + \gamma_{n2}$ ) in the lossy structure. The above calculated parameters are  $\gamma_1 = 5.39 \times 10^{11}$  Hz,  $\gamma'_1 = 8.69 \times 10^{10}$  Hz,  $\gamma_{r1} = 6.26 \times 10^{11}$  Hz,  $\gamma_{n1} = 6.85 \times 10^{11}$  Hz,  $\omega_1 = 1.23 \times 10^{15}$  Hz,  $r = 76\%$ ,  $t = 65\%$ ,  $\phi_1 = 203^\circ$ ,  $\phi_2 = 8^\circ$ ,  $\phi = 187^\circ$ ,  $\gamma_2 = \gamma'_2 = 4.12 \times 10^{12}$  Hz,  $\gamma_{n2} = 1.2 \times 10^{12}$  Hz, and  $\omega_2 = 1.245 \times 10^{15}$  Hz, respectively. The ratio between  $\gamma_1$  and  $\gamma'_1$  is 6.2, indicating high asymmetry in the coupling of the Mie modes with the two ports. The high reflection background mode transforms the Mie modes at 1530 nm into asymmetrically coupled Mie modes and decreases  $\gamma'_1$  due to the  $\cos(\phi)$  approaching  $-1$ . This key point enables the monolayer structure to break through the absorption limit of 50%. The yellow dashed line of Fig. 2(a) shows the absorption spectrum calculated using Eq. (1), derived based on TCMT. The result agrees well with the absorption spectrum simulated by the FDTD method. When the wavelength is smaller than 1500 nm, the absorption calculated by TCMT is significantly smaller than the FDTD method. This is because TCMT only includes the nonradiative decay rates at the resonance wavelengths, while the nonradiative decay rates are higher due to Ge having higher absorption coefficients at the short wavelength.

To get deep insight into the physical mechanism of the high reflection background mode at 1509 nm and resonance absorption at 1530 nm in this MMPA, multipole decompositions of the scattering cross sections (SCSs) of one unit cell in the metasurface are calculated. The modes of ED, toroidal dipole (TD), MD, electric quadrupole (EQ), and magnetic quadrupole (MQ) are calculated by the multipole decomposition method in a Cartesian coordinate system [32–34]. The details of the multipole decomposition method are described in Ref. [32] and the Appendix. The multipole components are calculated by extracting the induced current densities and substituting them into Eqs. (A7)–(A11). Figure 2(d) clearly shows that the contribution of the MD mode is dominated at the resonance wavelength of 1530 nm, indicating that the resonance absorption is mainly induced by the MD mode. Simultaneously, the EQ mode also provides a noticeable contribution to enhancing absorption, while the ED and MQ modes turn out to be weak. As shown in the inset of Fig. 2(d), the TD mode is excited at 1509 nm, providing a low- $Q$  but high reflection background over a broad spectral range and enhancing the absorption in a lossy structure. The excitation of the TD mode also transforms the MD and EQ modes into asymmetrically coupled Mie modes, resulting in different radiative decay rates for reflection and transmission, and decreases  $\gamma'_1$  due to the  $\cos(\phi)$  approaching  $-1$ . This enables the monolayer structure to break through the absorption limit of 50%. To further demonstrate that the TD mode induces the high reflection background, while the MD and EQ modes induce the absorption peak at 1530 nm, we plot the electromagnetic field distributions of the MMPA at resonance absorption peak wavelengths in Fig. 3. The white dashed lines sketch the geometry of the unit cell, and the arrows represent the field vectors that can confirm the existence of different Mie modes at resonance wavelengths. Figure 3(a) depicts the electric field distribution of the MMPA at 1509 nm in the  $\hat{x}$ – $\hat{y}$  plane. It can be observed that the electric field is mainly localized in the splits. The orientations of electric field vectors in the  $\hat{y}$  direction of neighboring split rings are

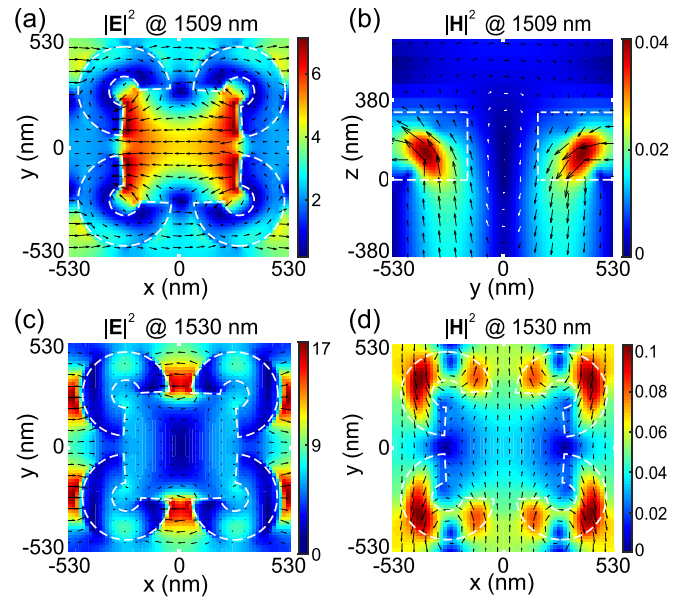


FIG. 3. Electromagnetic field distributions of the MMPA at resonance wavelength. Panels (a) and (b) show electric field distribution in the  $\hat{x}$ – $\hat{y}$  plane and magnetic field distribution in the  $\hat{y}$ – $\hat{z}$  plane at 1509 nm, respectively. Panels (c) and (d) show the electric field distribution and magnetic field distribution of the absorber in the  $\hat{x}$ – $\hat{y}$  plane at 1530 nm, respectively. The arrows represent the field vectors, and the white dashed lines sketch the geometry of the unit cell.

opposite, but the ones in the  $\hat{x}$  direction are the same. This indicates that opposite phase magnetic dipoles along the  $\hat{z}$  direction were induced in the  $\hat{y}$  direction neighboring split rings. Figure 3(b) shows the magnetic field distribution of MMPA at 1509 nm in the  $\hat{y}$ – $\hat{z}$  plane. It can be observed that the magnetic field is mainly localized in split rings. A head-to-tail magnetic moment is formed within the unit cell, indicating that the TD mode is excited along the  $\hat{y}$  direction [white arrows in Fig. 3(b)]. Figures 3(c) and 3(d) show the electric and magnetic field distributions at 1530 nm in the  $\hat{x}$ – $\hat{y}$  plane, respectively. From Fig. 3(c), the electric field is partially localized in four split rings and mainly localized in the gap between neighboring split rings along the  $\hat{x}$  direction, forming an electric quadrupole in the unit cell. The field vectors between neighboring split rings are with opposite signs, meaning that the EQ mode is excited at 1530 nm. The strong electric field, which is attributed to the near-field coupling of Mie modes of neighboring split rings, also enhances the absorption in the monolayer structure [35]. Figure 3(c) demonstrates that the magnetic field is localized in four split rings, with the field vectors circulating in a counterclockwise direction in SR1 and SR4, and in a clockwise direction in SR2 and SR3, indicating that the opposite phase electric dipoles along the  $\hat{z}$  direction are induced in the  $\hat{x}$  direction neighboring split rings and the MD mode is excited at 1530 nm. In all, the TD mode is excited at 1509 nm providing a low- $Q$  but high reflection background over a broad spectral range, transforming the MD and EQ modes excited at 1530 nm into asymmetrically coupled Mie modes, and decreasing  $\gamma'_1$  due to the  $\cos(\phi)$  approaching  $-1$ . The near-perfect absorption is

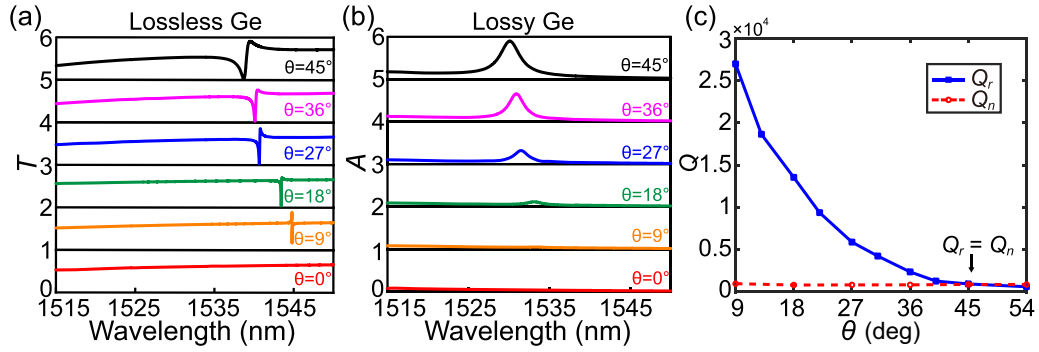


FIG. 4. Numerical results of (a) reflection spectra of the lossless structure and (b) absorption spectra of the lossy structure with different orientation angles  $\theta$ , respectively. (c) Theoretical results of  $Q$  factor  $Q_r$  (blue solid line) and nonradiative  $Q$  factor  $Q_n$  (red dashed line) of the absorber with different orientation angles  $\theta$ .

achieved in this monolayer structure due to critical coupling being satisfied at the resonance wavelength of 1530 nm.

To confirm the existence of a QBIC, which can tune the radiative decay rate of Mie modes to match the low nonradiative decay rate in MMPA, we perform numerical analysis of the transmission and absorption spectra at the wavelength range 1515–1555 nm in lossless and lossy structures, respectively. Figure 4(a) shows the transmission spectra with different orientation angles  $\theta$  in a lossless structure. When  $\theta = 0^\circ$ , the spectral linewidth of the resonance is vanished due to there being no perturbation in the structural symmetry, which cannot couple to the free space and correspond to BIC resonance with an infinity  $Q$  factor. By increasing  $\theta$ , the MD mode couples more into free space, hence broadening the spectral linewidth and blueshifting the position of resonance wavelength. The blue solid line in Fig. 4(c) shows the radiative  $Q$  factor ( $Q_r$ ) of lossless structure as a function of  $\theta$  extracted from Fig. 4(a). The relationship between the asymmetric parameter  $\theta$  and  $Q_r$  obeys the inverse square law, indicating that the radiative decay rate of Mie modes can be tuned to a large extent to match the low nonradiative decay rate. Figure 4(b) shows the absorption spectra with different orientation angles  $\theta$  in the lossy structure. At  $\theta = 0^\circ$ , the absorption bandwidth is vanishing, corresponding to the BIC resonance. While increasing  $\theta$ , both the total  $Q$  factor and the resonant wavelength decrease. The maximum absorption is achieved when the  $\theta = 45^\circ$ . The red dashed line in Fig. 4(c) shows the nonradiative  $Q$  factor ( $Q_n$ ) of the lossy structure. We can see that the orientation angle  $\theta$  has only a small impact on  $Q_n$  ( $\gamma_n$ ) because  $Q_n$  ( $\gamma_n$ ) is mainly determined by the absorption coefficient ( $n_2$ ) and geometric parameters of MMPA. Thus, the radiative decay rate of Mie modes can be adjusted by tuning orientation angle  $\theta$  to match the low nonradiative decay rate to achieve high- $Q$  near-perfect absorption at the critical coupling point.

#### IV. INFLUENCES OF GEOMETRIC PARAMETERS ON THE ABSORPTION

We then study the influences of geometric parameters on the performance of our proposed MMPA. The geometric parameters determine the Mie modes, which provide the opportunity to meet critical coupling condition at the resonance wavelength. Five important parameters, including the period

in the  $\hat{y}$  direction ( $p_y$ ), outer radius ( $r_1$ ), inner radius ( $r_2$ ), height ( $h$ ), and opening angle ( $\alpha$ ), are set as variables and their effects on the high- $Q$  near-perfect absorption are discussed in Fig. 5. The white-dashed lines show the optimal parameters to achieve high- $Q$  near-perfect absorption. Figure 5(a) displays the absorption spectrum of the MMPA by changing  $p_y$  from 900 to 1200 nm. By increasing the  $p_y$ , the TD background mode has a redshift, while the absorption peak has a blueshift due to the blueshift of MD and EQ modes. The bandwidth and maximum absorption increase first and then decrease with the increasing  $p_y$ . When  $p_y$  is near 1060 nm, the maximum absorption of the proposed MMPA can break through the absorption limit of 50%. These results are due to the TD background mode being excited near the resonance wavelength of the MD mode and decreasing  $\gamma'_1$ . The high- $Q$  near-perfect absorption can be achieved when  $p_y$  equals 1060 nm. The absorption spectrum for the MMPA by tuning the outer radius ( $r_1$ ) is shown in Fig. 5(b). The outer radius varies from 200 to 230 nm, while other geometric parameters of the unit cell are unchanged. The results show that the absorption peak has a redshift with increasing  $r_1$  due to the MD mode having redshifts. The bandwidth of the absorption spectrum increases due to the increases in the nonradiative decay rate as  $r_1$  increases. The maximum absorption over the entire spectrum increases first and then decreases because increasing  $r_1$  causes MMPA to change from overcoupling ( $\gamma_{r1} > \gamma_{n1}$ ) to critical coupling ( $\gamma_{r1} = \gamma_{n1}$ ) and then to undercoupling ( $\gamma_{r1} < \gamma_{n1}$ ). There is a tradeoff between bandwidth and maximum absorption. The high- $Q$  near-perfect absorption is achieved in MMPA when  $r_1$  equals 213 nm. Figure 5(c) presents the absorption spectrum of the MMPA by increasing the inner radius ( $r_2$ ) of split rings from 30 to 90 nm. A blueshift of absorption peak is found due to the MD mode being blueshifted. The bandwidth decreases slightly with the increasing  $r_2$  due to the slightly decreasing radiative and nonradiative decay rate. The maximum high- $Q$  absorption is achieved when  $r_2$  is 66 nm. Figure 5(d) shows the absorption spectrum for the absorber by tuning the height ( $h$ ) of the split rings from 235 to 245 nm. It can be seen that the position of the absorption peak has a redshift because of the redshift of the MD mode. As the height increases, both the bandwidth and maximum absorption decrease slightly due to the MD mode redshift and moving away from the TD

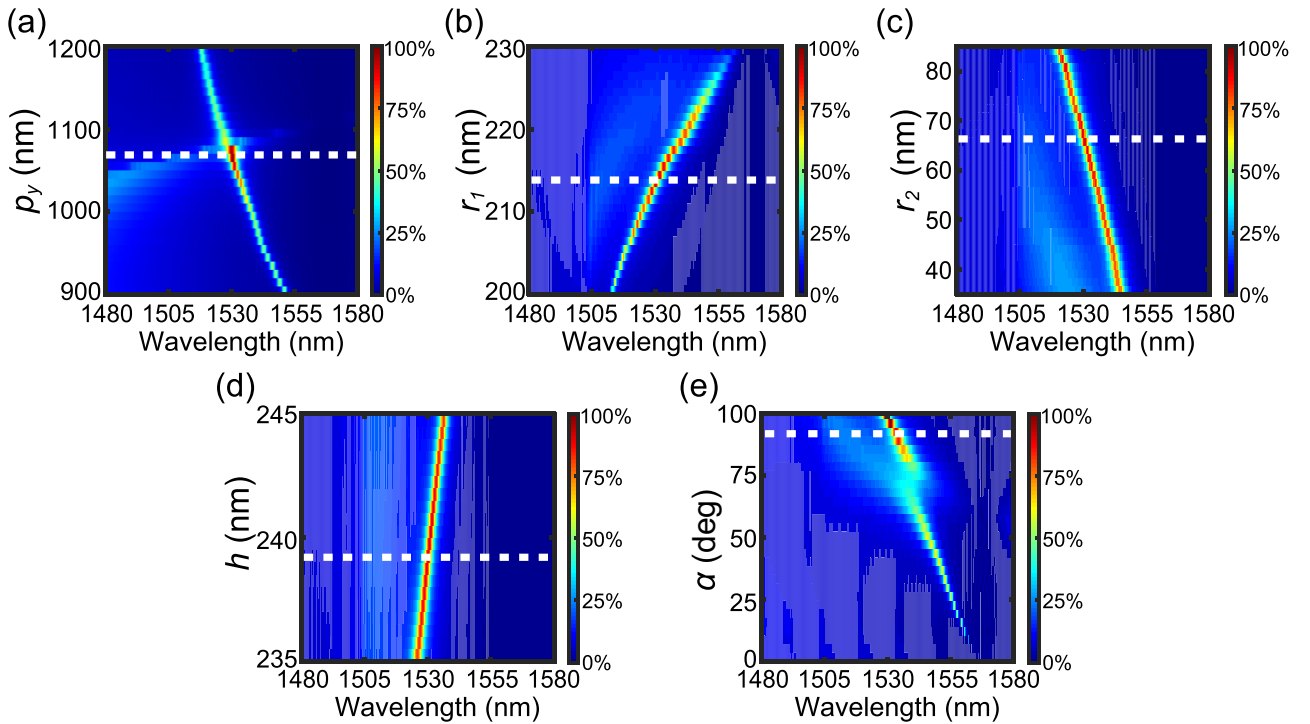


FIG. 5. Absorption spectra of the structure for varying (a) period in the  $\hat{y}$  direction from 900 to 1200 nm, (b) outer radius from 200 to 230 nm, (c) inner radius from 30 to 90 nm, (d) height from 235 to 245 nm, and (e) opening angle from  $0^\circ$  to  $100^\circ$ , respectively. The white dashed lines in (a)–(e) show the optimal parameters to achieve high- $Q$  near-perfect absorption.

background mode. The high- $Q$  near-perfect absorption can be achieved when the height equals 239 nm. Figure 5(e) shows the absorption spectra by turning the opening angle ( $\alpha$ ) from  $0^\circ$  to  $100^\circ$ . While increasing  $\alpha$ , the absorption peak has a blueshift due to the blueshift of TD and MD modes. The bandwidth increases because the radiative decay rate of TD and MD modes increases. The maximum absorption can break through the limit of 50% when  $\alpha$  is greater than  $80^\circ$  due to the MD mode being excited near the resonance wavelength of the TD background mode. The high- $Q$  near-perfect absorption can be achieved when the opening angle is  $96^\circ$ . Therefore, by adjusting the geometric parameters of the MMPA, radiative and nonradiative decay rates can be adjusted to achieve a better high- $Q$  absorption performance.

## V. CONCLUSIONS

In conclusion, we have proposed a high- $Q$  near-perfect absorber based on a monolayer all-dielectric metasurface without the back reflectors, in which the maximum absorption is as high as 93%, and the value of the  $Q$  factor is up to 470. This structure is polarization independent due to its  $C_4$  symmetry. By tuning the orientation angle of each split ring, the Mie modes with low radiative decay rates are induced to match the low nonradiative decay and achieve high- $Q$  absorption performance. Based on the TCMT, we demonstrate that the high reflection background mode excited by four split rings in one unit cell can transform the symmetrically coupled Mie modes into asymmetrically coupled ones and decrease the radiative decay rate of transmission, enabling the mono-

layer structure to break through the absorption limit of 50%. Furthermore, the effects of geometric parameters of the metasurface on absorption characteristics are also explored. Our proposed monolayer all-dielectric structure has great potential in ultrafast optoelectronic devices and integrated photon systems.

## ACKNOWLEDGMENTS

This work was supported by the Key Project of the National Key R&D Program of China (Grant No. 2022YFA1404500), the National Natural Science Foundation of China (Grants No. 12074186, No. 11734012, and No. 12074267), and the Science and Technology Project of Guangdong, China (Grant No. 2020B010190001).

## APPENDIX: MULTIPOLE DECOMPOSITION METHOD

Multipole decomposition was employed to analyze the different Mie modes excited inside the resonators. When incident light irradiates the resonator or resonators array, the induced current density distributions  $\mathbf{J}$  can be obtained from the electric field distributions  $\mathbf{E}(\mathbf{r})$  by

$$\mathbf{J}(\mathbf{r}) = -i\omega\epsilon_0(n^2 - 1)\mathbf{E}(\mathbf{r}), \quad (\text{A1})$$

where  $\epsilon_0$  is the permittivity of free space,  $\omega$  is the angular frequency, and  $n$  is the refractive profile of the resonators. The possible presence of a substrate is fully considered by



this approach. The moments of ED ( $\mathbf{p}$ ), TD ( $\mathbf{T}$ ), MD ( $\mathbf{m}$ ), EQ ( $\hat{\mathbf{Q}}^e$ ), and MQ ( $\hat{\mathbf{Q}}^m$ ) can be derived as

$$p_\alpha = -\frac{1}{i\omega} \int J_\alpha d^3\mathbf{r}, \quad (\text{A2})$$

$$T_\alpha = \frac{1}{10c} \int \{(\mathbf{r} \cdot \mathbf{J})r_\alpha - 2r^2 J_\alpha\} d^3\mathbf{r}, \quad (\text{A3})$$

$$m_\alpha = \frac{1}{2} \int (\mathbf{r} \times \mathbf{J})_\alpha d^3\mathbf{r}, \quad (\text{A4})$$

$$\begin{aligned} \hat{Q}_{\alpha\beta}^e = & -\frac{1}{i\omega} \left\{ \int [3(r_\beta J_\alpha + r_\alpha J_\beta) - 2(\mathbf{r} \cdot \mathbf{J})\delta_{\alpha\beta}] d^3\mathbf{r} \right. \\ & + \frac{k^2}{14} \int [4r_\alpha r_\beta (\mathbf{r} \cdot \mathbf{J}) - 5r^2 (r_\alpha J_\beta + r_\beta J_\alpha) \\ & \left. + 2r^2 (\mathbf{r} \cdot \mathbf{J})\delta_{\alpha\beta}] d^3\mathbf{r} \right\}, \quad (\text{A5}) \end{aligned}$$

$$\hat{Q}_{\alpha\beta}^m = \int \{r_\alpha (\mathbf{r} \times \mathbf{J})_\beta + r_\beta (\mathbf{r} \times \mathbf{J})_\alpha\} d^3\mathbf{r}, \quad (\text{A6})$$

respectively, where  $r$  is the radius vector of a volume element inside the resonator,  $c$  is the speed of light in vacuum,  $\alpha, \beta = x, y, z$ , and  $k$  is the wave number, respectively. The SCSs of multipoles can be expressed as

$$C_{\text{ED}} = \frac{k^4}{6\pi\epsilon_0^2|\mathbf{E}_{\text{inc}}|} \sum (|\mathbf{p}|^2), \quad (\text{A7})$$

$$C_{\text{TD}} = \frac{k^4}{6\pi\epsilon_0^2|\mathbf{E}_{\text{inc}}|} \sum |ik\mathbf{T}|^2, \quad (\text{A8})$$

$$C_{\text{MD}} = \frac{k^4}{6\pi\epsilon_0^2|\mathbf{E}_{\text{inc}}|} \sum \left| \frac{\mathbf{m}}{c} \right|^2, \quad (\text{A9})$$

$$C_{\text{EQ}} = \frac{k^4}{720\pi\epsilon_0^2|\mathbf{E}_{\text{inc}}|} \sum (|\hat{\mathbf{Q}}^e|^2), \quad (\text{A10})$$

$$C_{\text{MQ}} = \frac{k^4}{720\pi\epsilon_0^2|\mathbf{E}_{\text{inc}}|} \sum \left( \left| \frac{k\hat{\mathbf{Q}}^m}{c} \right|^2 \right), \quad (\text{A11})$$

where  $\mathbf{E}_{\text{inc}}$  denotes the incident electric field.

- [1] N. Yu, P. Genevet, M. A. Kats, F. Aieta, J.-P. Tetienne, F. Capasso, and Z. Gaburro, Light propagation with phase discontinuities: Generalized laws of reflection and refraction, *Science* **334**, 333 (2011).
- [2] L. Feng, P. Huo, Y. Liang, and T. Xu, Photonic metamaterial absorbers: Morphology engineering and interdisciplinary applications, *Adv. Mater.* **32**, 1903787 (2020).
- [3] N. Liu, M. Mesch, T. Weiss, M. Hentschel, and H. Giessen, Infrared perfect absorber and its application as plasmonic sensor, *Nano Lett.* **10**, 2342 (2010).
- [4] H. Zhang and K. Wu, Ultra-broadband near-perfect absorber based on a single-layer Ge-assisted metasurface, *J. Opt. Soc. Am. B* **39**, 332 (2022).
- [5] A. Lochbaum, Y. Fedoryshyn, A. Dorodnyy, U. Koch, C. Hafner, and J. Leuthold, On-chip narrowband thermal emitter for mid-IR optical Gas sensing, *ACS Photonics* **4**, 1371 (2017).
- [6] W. Wang, L. V. Besteiro, P. Yu, F. Lin, A. O. Govorov, H. Xu, and Z. Wang, Plasmonic hot-electron photodetection with quasi-bound states in the continuum and guided resonances, *Nanophotonics* **10**, 1911 (2021).
- [7] Z. Shen, X. Fang, S. Li, W. Yin, L. Zhang, and X. Chen, Terahertz spin-selective perfect absorption enabled by quasi-bound states in the continuum, *Opt. Lett.* **47**, 505 (2022).
- [8] J. Tian, H. Luo, Q. Li, X. Pei, K. Du, and M. Qiu, Near-infrared super-absorbing all-dielectric metasurface based on single-layer germanium nanostructures, *Laser Photonics Rev.* **12**, 1800076 (2018).
- [9] C. Yang, J. Yang, Z. Yang, Z. Zhou, M. Sun, V. E. Babicheva, and K. Chen, Nonradiating silicon nanoantenna metasurfaces as narrowband absorbers, *ACS Photonics* **5**, 2596 (2018).
- [10] H. Luo, J. Tian, Q. Li, B. Ma, Y. Zhu, J. Yu, Y. Hong, A. Ouyang, P. Belov, R. K. Sinha, S. Kaur, and M. Qiu, Flat photonics for broadband light-trapping, *Appl. Phys. Lett.* **117**, 241105 (2020).
- [11] Y. Cai, X. Liu, K. Zhu, H. Wu, and Y. Huang, Enhancing light absorption of graphene with dual quasi bound states in the continuum resonances, *J. Quant. Spectrosc. Radiat. Transfer* **283**, 108150 (2022).
- [12] C. W. Hsu, B. Zhen, A. D. Stone, J. D. Joannopoulos, and M. Soljačić, Bound states in the continuum, *Nat. Rev. Mater.* **1**, 16048 (2016).
- [13] X. Wang, J. Duan, W. Chen, C. Zhou, T. Liu, and S. Xiao, Controlling light absorption of graphene at critical coupling through magnetic dipole quasi-bound states in the continuum resonance, *Phys. Rev. B* **102**, 155432 (2020).
- [14] T. Zeng, G. Liu, L. Wang, and Q. Lin, Light-matter interactions enhanced by quasi-bound states in the continuum in a graphene-dielectric metasurface, *Opt. Express* **29**, 40177 (2021).
- [15] J. Yu, B. Ma, R. Qin, P. Ghosh, M. Qiu, and Q. Li, High-Q absorption in all-dielectric photonics assisted by metamirrors, *ACS Photonics* **9**, 3391 (2022).
- [16] J. Wang, J. Yang, H. Zhao, and M. Chen, Quasi-BIC-governed light absorption of monolayer transition-metal dichalcogenide-based absorber and its sensing performance, *J. Phys. D: Appl. Phys.* **54**, 485106 (2021).
- [17] K. Koshelev, S. Lepeshov, M. Liu, A. Bogdanov, and Y. Kivshar, Asymmetric Metasurfaces with High-Q Resonances Governed by Bound States in the Continuum, *Phys. Rev. Lett.* **121**, 193903 (2018).
- [18] J. Tian, Q. Li, P. A. Belov, R. K. Sinha, W. Qian, and M. Qiu, High-Q all-dielectric metasurface: Super and suppressed optical absorption, *ACS Photonics* **7**, 1436 (2020).
- [19] S. Wan, C. Qin, K. Wang, Y. Li, C. Guan, B. Lv, W. Li, and J. Shi, Ultra-high quality perfect absorber based on quasi bound states in the continuum, *J. Appl. Phys.* **131**, 213104 (2022).
- [20] R. Masoudian Saadabad, L. Huang, and A. E. Miroshnichenko, Polarization-independent perfect absorber enabled by quasi-bound states in the continuum, *Phys. Rev. B* **104**, 235405 (2021).
- [21] F. Wu, D. Liu, and S. Xiao, Bandwidth-tunable near-infrared perfect absorption of graphene in a compound grating waveguide structure supporting quasi-bound states in the continuum, *Opt. Express* **29**, 41975 (2021).
- [22] W. Liu, Z. Liang, Z. Qin, X. Shi, F. Yang, and D. Meng, Polarization-insensitive dual-band response governed by quasi bound states in the continuum for high-performance refractive index sensing, *Results Phys.* **32**, 105125 (2022).



- [23] O. Mitrofanov, L. L. Hale, P. P. Vabishchevich, T. S. Luk, S. J. Addamane, J. L. Reno, and I. Brener, Perfectly absorbing dielectric metasurfaces for photodetection, *APL Photonics* **5**, 101304 (2020).
- [24] I. Koirala, S.-S. Lee, and D.-Y. Choi, Highly transmissive subtractive color filters based on an all-dielectric metasurface incorporating TiO<sub>2</sub> nanopillars, *Opt. Express* **26**, 18320 (2018).
- [25] A. Kodigala, T. Lepetit, Q. Gu, B. Bahari, Y. Fainman, and B. Kanté, Lasing action from photonic bound states in continuum, *Nature (London)* **541**, 196 (2017).
- [26] K. X. Wang, Z. Yu, S. Sandhu, and S. Fan, Fundamental bounds on decay rates in asymmetric single-mode optical resonators, *Opt. Lett.* **38**, 100 (2013).
- [27] A. Taflov and S. C. Hagness, *Computational Electromagnetics: The Finite-Difference Time-Domain Method*, 2nd ed. (Artech House, Norwood, 2000).
- [28] K. Wu, P. Coquet, Q. J. Wang, and P. Genevet, Modelling of free-form conformal metasurfaces, *Nat. Commun.* **9**, 3494 (2018).
- [29] D. H. Raguin and G. M. Morris, Antireflection structured surfaces for the infrared spectral region, *Appl. Opt.* **32**, 1154 (1993).
- [30] K. Wu and G. P. Wang, One-dimensional Fibonacci grating for far-field super-resolution imaging, *Opt. Lett.* **38**, 2032 (2013).
- [31] E. D. Palik, in *Handbook of Optical Constants of Solids* (Academic, New York, 1998), Vol. I, pp. 465–478.
- [32] R. Alaee, C. Rockstuhl, and I. Fernandez-Corbaton, An electromagnetic multipole expansion beyond the long-wavelength approximation, *Opt. Commun.* **407**, 17 (2018).
- [33] V. Savinov, V. A. Fedotov, and N. I. Zheludev, Toroidal dipolar excitation and macroscopic electromagnetic properties of metamaterials, *Phys. Rev. B* **89**, 205112 (2014).
- [34] T. Hinamoto and M. Fujii, MENP: An open-source MATLAB implementation of multipole expansion for nanophotonics, *OSA Continuum* **4**, 1640 (2021).
- [35] S. Lepeshov and Y. Kivshar, Near-field coupling effects in Mie-resonant photonic structures and all-dielectric metasurfaces, *ACS Photonics* **5**, 2888 (2018).